LRIP-Net: Low-Resolution Image Prior based Network for Limited-Angle CT Reconstruction

Qifeng Gao, Rui Ding, Linyuan Wang*, Bin Xue, and Yuping Duan*

***Abstract*—In the practical applications of computed tomography imaging, the projection data may be acquired within a limited-angle range and corrupted by noises due to the limitation of scanning conditions. The noisy incomplete projection data results in the ill-posedness of the inverse problems. Based on the observation that the low-resolution reconstruction problem has better numerical stability, we propose a novel low-resolution image prior based CT reconstruction model for limited-angle reconstruction. More specifically, we build up a low-resolution reconstruction problem on the down-sampled projection data, and use the reconstructed low-resolution image as prior knowledge for the high-resolution limited-angle CT problem. The constrained minimization problem is then solved by the alternating direction method with all sub-minimization problems approximated by the convolutional neural networks. Numerical experiments demonstrate that our double-resolution network outperforms both the variational method and popular learning-based reconstruction methods on noisy limited-angle reconstruction problems.**

***Index Terms*—Computed tomography, inverse problem, ill-posedness, limited-angle, deep unrolling**

I. INTRODUCTION

X-RAY Computed Tomography (CT) is widely used for clinical diagnosis, the quality of which directly affects the judgment of the clinicians. The filtered back-projection (FBP), algebraic reconstruction technique (ART), and simultaneous algebraic reconstruction technique (SART) are popular choices for the full scanned CT data. However, the imaging system may collect incomplete projection data due to the system's geometric limitations and other factors. It was proven that the reconstruction problem becomes highly unstable with scanning angular range less than $2\pi/3$. For more background, we refer to [17] and references therein. The aforementioned degenerated scanned data makes the direct method and iterative methods suffer from severe streaking artifacts and noise-induced artifacts [18], [21]. For limited-angle CT reconstruction, various algorithms were proposed, which can be broadly categorized into the regularization-based method and learning-based method.

The regularization-based method has been applied to the improperly posed problems and achieved great successes, which are good choices for the limited-angle CT reconstruction problems. Since compressed sensing (CS) was proposed by Candes, Romberg and Tao [9], various models and algorithms have been proposed to improve the reconstruction quality using the total variation (TV) for image reconstruction problems [10], [28]. Sidky and Pan [33] developed the primal-dual algorithm for solving the TV minimization problem, which performed well concerning angular under-sampling reconstruction. Ritschl *et al.* [32] presented a new method for optimized parameter adaption for sparsity constrained image reconstruction. Chen *et al.* [12] proposed the anisotropic TV minimization method, which performed better than the isotropic TV model for the limited-angle CT reconstruction. Frikel [17] used the sparse regularization technique in combination with curvelets to realize an edge-preserving reconstruction. Cai *et al.* [7] developed an edge guided total variation minimization reconstruction algorithm in dealing with high quality image reconstruction. Xu *et al.* [39] combined the ℓ_1 norm of gradient and ℓ_0 norm of gradient as the regularization term and developed the efficient alternating edge-preserving diffusion and smoothing algorithm, which can well preserve the edges for limited-angle reconstruction problem.

In addition to TV-based regularization methods, high-order regularization methods have also been investigated for degenerated scanned data. Niu *et al.* [30] presented a penalized weighted least-squares scheme to retain the image quality by incorporating the total generalized variation regularization. Zhang *et al.* [43] introduced the curvature-driven Euler's elastica regularization to rectify large curvatures and kept the isophotes smooth without erratic distortions. Cai *et al.* [8] proposed the block matching sparsity regularization for CT image reconstruction for an incomplete projection set. Wang *et al.* [37] presented the guided image filtering-based limited-angle CT reconstruction algorithm using wavelet frame. Xu *et al.* [40] combined the dictionary learning and image gradient ℓ_0-norm into image reconstruction model for limited-angle CT reconstruction. Wang *et al.* [36] considered minimizing the ℓ_1/ℓ_2 term on the gradient for a limited-angle scanning problem in CT reconstruction. However, the aforementioned regularization methods are usually time-consuming and suffer

---

This work did not involve human subjects or animals in its research. All authors declare that they have no known conflicts of interest in terms of competing financial interests or personal relationships that could have an influence or are relevant to the work reported in this paper. The work was partially supported by the National Natural Science Foundation of China (NSFC 12071345, 11701418), Major Science and Technology Project of Tianjin 18ZXRHSY00160, and Recruitment Program of Global Young Expert. The fourth author B Xue was supported by the National Natural Science Foundation of China (NSFC 62075162, 62001329) and Natural Science Foundation of Tianjin 19JCQNJC01700. *Asterisk indicates the corresponding author.*

Qifeng Gao is with the Center for Applied Mathematics, Tianjin University, Tianjin 300072, China (e-mail: gaoqifeng_98@tju.edu.cn).

Rui Ding is with the Center for Applied Mathematics, Tianjin University, Tianjin 300072, China (e-mail: d18822058320@163.com).

Linyuan Wang is with Henan Key Laboratory of Imaging and Intelligent Processing, PLA Strategy Support Force Information Engineering University, Zhengzhou 450002, China (e-mail:wanglinyuanwly@163.com).

Bin Xue is with the School of Marine Science and Technology, TianJin University, Tianjin 30072, China (e-mail: xuebin@tju.edu.cn).

Yuping Duan is with the Center for Applied Mathematics, Tianjin University, Tianjin 300072, China (e-mail: yuping.duan@tju.edu.cn).

from tricky parameter tuning.

Due to the development of deep convolutional neural networks (CNNs) in a broad range of computer vision tasks, deep learning methods become more and more popular in the medical imaging field. With regard to limited-angle CT reconstruction, Pelt and Batenburg [31] proposed an artificial neural network-based fast limited-angle image reconstruction algorithm, which can be regarded as a weighted combination of the FBP method and some learned filters. Boublil *et al.* [4] utilized a CNN-based model to integrate multiple reconstructed results. Kang *et al.* [26] constructed a deep CNN model in the wavelet domain, which trained the wavelet coefficients from the CT images after applying the contourlet transform. Gupta *et al.* [19] presented a new image reconstruction method, which replaced the projector in a projected gradient descent with a CNN. Adler and Öktem [1] proposed a deep neural network by unrolling a proximal primal-dual optimization method and replacing the proximal operators with a CNN. Chen *et al.* [11] unfolded the field of experts regularized CT reconstruction model into a deep learning network, all parameters of which can be learned from the training process. Han and Ye [20] proposed a new multi-resolution deep learning scheme based on the frame condition to overcome the limitation of U-net. Zhang *et al.* [44] presented a new deep CNN jointly reconstructs CT images and their associated Radon domain projections, and constructed a hybrid loss function to effectively protect the important structure of images. Bubba *et al.* [6] developed a hybrid reconstruction framework that fused model-based sparse regularization with data-driven deep learning to solve the severely ill-posed inverse problem of limited-angle CT. Arridge *et al.* [2] attempted to provide an overview of methods for integrating data-driven concepts into the field of inverse problems and a solid mathematical theory. Würfl *et al.* [38] mapped the Feldkamp-Davis-Kress algorithm to the neural networks by introducing a novel cone-beam back-projection layer for limited-angle problems. Lin *et al.* [27] proposed an end-to-end trainable dual-domain network to simultaneously restore sinogram consistency and enhance CT images. Baguer *et al.* [3] introduced the deep image prior approach in combination with classical regularization and an initial reconstruction. Ding *et al.* [14] came up with a method based on the unrolling of a proximal forward-backward splitting framework with a data-driven image regularization via deep neural networks. Cheng *et al.* [13] proposed a novel reconstruction model to jointly reconstruct a high-quality image and its corresponding high-resolution projection data. Zang *et al.* [42] proposed IntraTomo, a powerful framework that combines the benefits of learning-based and model-based approaches for solving highly ill-posed inverse problems. Hu *et al.* [22] developed a method termed Single-shot Projection Error Correction Integrated Adversarial Learning (SPECIAL) progressive-improvement strategy, which could effectively combine the complementary information contained in the image domain and projection domain. Bubba *et al.* [5] proposed a novel CNN, designed for learning pseudodifferential operators in the context of linear inverse problems. Hu *et al.* [23] proposed a novel reconstruction framework termed Deep Iterative Optimization-based Residual-learning (DIOR) for limited-angle CT, which combined iterative optimization and deep learning based on the residual domain. Although the aforementioned learning-based methods have achieved better reconstruction results than the regularization-based methods, the high ill-posedness of the limited-angle reconstruction problems still challenges the reconstruction quality.

The incomplete projection data makes the inverse problem towards the ill-posedness, becoming more and more sensitive to noises. We observe that the low-resolution reconstruction problems have better numerical stability than the corresponding high-resolution reconstruction problems. Therefore, we propose a novel low-resolution image prior based trainable reconstruction approach for the limited-angle CT reconstruction. More specifically, we use the established reconstruction method to obtain the low-resolution image from the down-sampled raw measured data. In what follows, we build up the constrained reconstruction problem, which is solved by the alternating direction method. By approximating the resolvent operators by CNNs, an end-to-end algorithm is gained to reconstruct images from raw data. We evaluate the performance of the proposed method on the American Association of Physicists in Medicine (AAPM) Challenge dataset. By comparing with the state-of-the-art reconstruction methods, our algorithm is shown more effective in dealing with limited-angle data contaminated by either Gaussian or Poisson noises.

The rest of the paper is organized as follows. We present the double-resolution reconstruction method in Section II. Section III is dedicated to explaining the details of our network architecture, loss function, and optimization. We present the numerical results on AAPM phantom CT dataset corrupted by Gaussian noises and Poisson noises in Section IV. Finally, a brief conclusion and possible future works are presented in Section V.

II. THE DOUBLE-RESOLUTION RECONSTRUCTION METHOD

A. *Double-resolution reconstruction model*

The CT reconstruction problem aims to reconstruct clean image $\boldsymbol{u} \in X$ from the projection data $\boldsymbol{f} \in Y$ with unknown noise $\boldsymbol{\delta} \in Y$, whose mathematical formulation is:

$$\boldsymbol{f} = A\boldsymbol{u} + \boldsymbol{\delta}, \tag{1}$$

where the reconstruction space X and the data space Y are typically Hilbert Spaces, $A : X \to Y$ is the forward operator that models how an image gives rise to data in absence of noise. When the light source is a fan beam, the dimension of the system matrix is $M \times N$ with M and N given as follows

$$M = N_{\text{views}} \times N_{\text{bins}}, \quad \text{and} \quad N = n \times n,$$

where N_{views} denotes the number of angles in the angular interval for limited-angle CT reconstruction, N_{bins} denotes the number of units on the detector, and N represents the number of pixels of the input image. For CT reconstruction problem (1), the condition number of the system matrix A directly affects the stability of the solution [25]. The larger the condition number of the system matrix, the more serious the ill-posedness of the inverse problem, which may result in the degradation of the numerical methods.

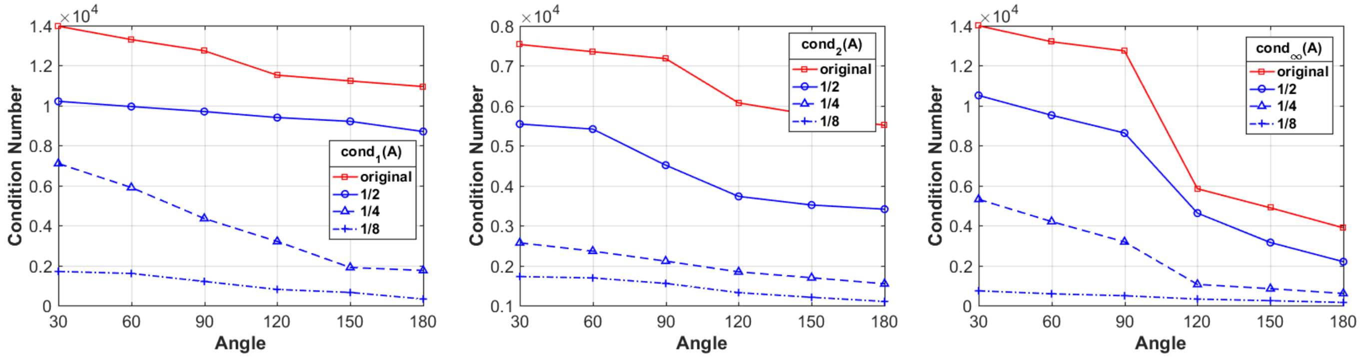

(a) Condition number by 1-norm (b) Condition number by 2-norm (c) Condition number by ∞-norm

Fig. 1. The condition number comparison for the system matrices with different image resolutions, where the down-sampling rate is used as 1/2, 1/4, and 1/8, respectively.

We investigate the condition numbers of the system matrix with different image resolutions. More specifically, we define the low-resolution image using the equidistant sampling with the step size of τ. Then the dimension of the low-resolution image u_l becomes $n/\tau \times n/\tau$. For the low-resolution system matrix A_l, the geometric parameters are consistent with the original system matrix A, i.e., the N_{views} and N_{bins} of A_l being the same as A, and only the number of pixels changes. The dimension of the low-resolution system matrix A_l becomes $M \times N/\tau^2$. As shown in Fig. 1, we evaluate the condition numbers of the system matrices on the limited-angle reconstruction problem, where the angle range varies from 180° to 30°. We can observe that no matter which norm is used to calculate the condition number, the smaller the resolution of the image is, the smaller the condition number is.

Since large condition numbers lead to numerical instability and severe sensitivity to noisy measurements [25], the low-resolution image can be used as prior to improve the solution of limited-angle CT reconstruction, where the low-resolution image can be expressed by the down-sampling matrix D as given below

$$\boldsymbol{u}_l = D\boldsymbol{u},$$

where $\boldsymbol{u}_l$ is the down-sampled image and $D^T D$ is a diagonal matrix with diagonal elements being either 1 or 0. Considering this, we propose the following constrained minimization problem for CT reconstruction

$$\begin{aligned} \min_{u} \quad & \mathcal{F}(A\boldsymbol{u}, f) + \mathcal{R}(\boldsymbol{u}) \\ \text{s.t.} \quad & D\boldsymbol{u} = \boldsymbol{u}_l, \end{aligned} \tag{2}$$

where $\mathcal{F}(\cdot)$ denotes the data fidelity term, and $\mathcal{R}(\cdot)$ denotes the regularization term.

B. Learned alternating direction algorithm

The constrained minimization problem (2) can be further reformulated into an unconstrained minimization problem using the penalty method as follows

$$\min_{\boldsymbol{u}} \quad \mathcal{F}(A\boldsymbol{u}, \boldsymbol{f}) + \mathcal{R}(\boldsymbol{u}) + \frac{1}{2\mu}\left\|D\boldsymbol{u} - \boldsymbol{u}_l\right\|_2^2, \tag{3}$$

where μ is a positive regularization parameter. Because all terms in (3) contain the variable $\boldsymbol{u}$ making the minimization task difficult, we introduce an auxiliary variable $\tilde{\boldsymbol{u}}$ and rewrite (3) as the following minimization problem

$$\min_{\boldsymbol{u},\tilde{\boldsymbol{u}}} \mathcal{F}(A\tilde{\boldsymbol{u}}, \boldsymbol{f}) + \mathcal{R}(\tilde{\boldsymbol{u}}) + \frac{1}{2\mu}\left\|D\boldsymbol{u} - \boldsymbol{u}_l\right\|_2^2 + \frac{1}{2r}\left\|\tilde{\boldsymbol{u}} - \boldsymbol{u}\right\|_2^2,$$

where r is a positive parameter. The main advantage of above minimization problem is that we can use the alternating direction method to solve the multi-variable minimization problem. The variables $\tilde{\boldsymbol{u}}$ and $\boldsymbol{u}$ can be estimated alternatively by solving the following two energy minimization problems

$$\min_{\tilde{\boldsymbol{u}}} \quad \mathcal{F}(A\tilde{\boldsymbol{u}}, \boldsymbol{f}) + \mathcal{R}(\tilde{\boldsymbol{u}}) + \frac{1}{2r}\left\|\tilde{\boldsymbol{u}} - \boldsymbol{u}\right\|_2^2, \tag{4}$$

and

$$\min_{\boldsymbol{u}} \quad \frac{1}{2r}\left\|\tilde{\boldsymbol{u}} - \boldsymbol{u}\right\|_2^2 + \frac{1}{2\mu}\left\|D\boldsymbol{u} - \boldsymbol{u}_l\right\|_2^2, \tag{5}$$

respectively. The minimization (4) is a typical regularization model, which can be solved by the learned primal-dual algorithm as follows

$$\begin{cases} \boldsymbol{p}^{k+1} = \arg\min\limits_{\boldsymbol{p}} \mathcal{F}^*(\boldsymbol{p}, \boldsymbol{f}) - \left\langle A\tilde{\boldsymbol{u}}^k, \boldsymbol{p}\right\rangle + \frac{1}{2\tau}\left\|\boldsymbol{p} - \boldsymbol{p}^k\right\|_2^2, \\ \tilde{\boldsymbol{u}}^{k+1} = \arg\min\limits_{\tilde{\boldsymbol{u}}} \mathcal{R}(\tilde{\boldsymbol{u}}) + \left\langle A\tilde{\boldsymbol{u}}, \boldsymbol{p}^{k+1}\right\rangle + \frac{1}{2\tau}\left\|\tilde{\boldsymbol{u}} - \boldsymbol{u}^k\right\|_2^2, \end{cases}$$

where $\mathcal{F}^*$ denotes the adjoint operator of $\mathcal{F}$, $\boldsymbol{p}$ is the dual variable of $\tilde{\boldsymbol{u}}$, τ is a positive parameter. On the other hand, the minimization problem (5) is a least squared problem, which can be solved by the closed-form solution. To sum up, we propose to use the following iterative scheme to solve the minimization problem (4) and (5) in an alternative way

$$\begin{cases} \boldsymbol{u}^{k+1} = (\mu\mathcal{I} + rD^*D)^{-1}(\mu\tilde{\boldsymbol{u}}^k, rD^*\boldsymbol{u}_l), \\ \boldsymbol{p}^{k+1} = (\mathcal{I} + \tau\partial\mathcal{F}^*)^{-1}(\boldsymbol{p}^k, A\tilde{\boldsymbol{u}}^k, \boldsymbol{f}), \\ \tilde{\boldsymbol{u}}^{k+1} = (\mathcal{I} + r\partial\mathcal{R})^{-1}(\boldsymbol{u}^k, A^*\boldsymbol{p}^{k+1}), \end{cases} \tag{6}$$

where $\mathcal{I}$ denotes the identity operator, A^* and D^* represent the adjoint operators of the forward operator A and down-sampling operator D, respectively.

In the followings, we intend to summarize the unrolled alternating direction algorithm by the deep neural networks to solve the low-resolution image prior based CT reconstruction model (2); see Algorithm 1. In the algorithm, we use the total

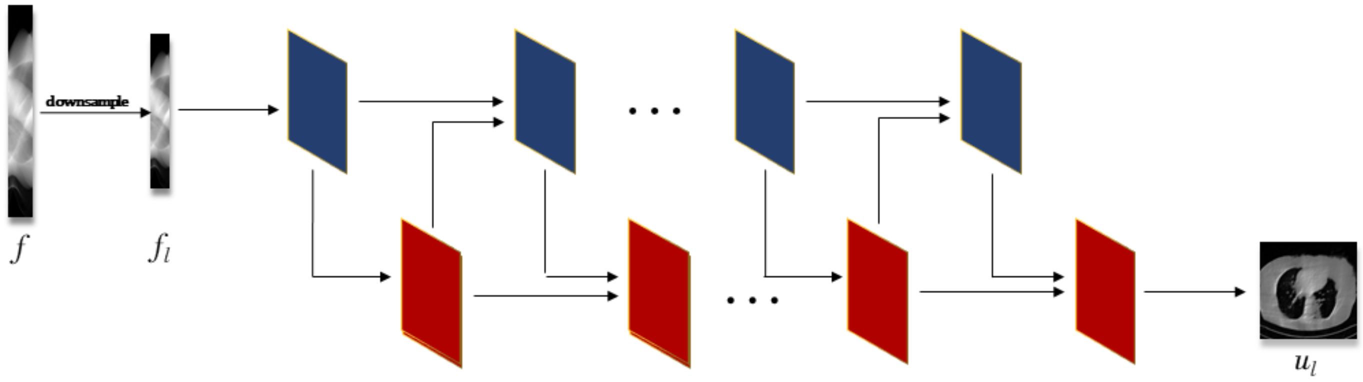

Fig. 2. The network of low-resolution reconstruction model. The down-sampled projection data is reconstructed using the learned primal-dual algorithm to obtain the low-resolution image, where the proximal operators have been replaced with CNNs, and each block is composed of three convolution layers, PReLU and residual connection.

I iterations to build up the Low-Resolution Image Prior based network, which is shorted as LRIP-net in our work.

Algorithm 1 The Low-Resolution Image Prior based Network

```
Initialize $\boldsymbol{p}^0$, $\boldsymbol{u}^0$, $\tilde{\boldsymbol{u}}^0$
for $k = 0,\ldots, I$, do
    $\boldsymbol{u}^{k+1} \leftarrow \Pi_{\theta^{\boldsymbol{u}}}(\tilde{\boldsymbol{u}}^k, D^*\boldsymbol{u}_l)$;
    $\boldsymbol{p}^{k+1} \leftarrow \Gamma_{\theta^{\boldsymbol{p}}}(\boldsymbol{p}^k, A\tilde{\boldsymbol{u}}^k, \boldsymbol{f})$;
    $\tilde{\boldsymbol{u}}^{k+1} \leftarrow \Lambda_{\theta^{\tilde{\boldsymbol{u}}}}(\boldsymbol{u}^{k+1}, A^*\boldsymbol{p}^{k+1})$;
return $\boldsymbol{u}^I$
```

Remark 1. *We assume the constraint* $\tilde{\boldsymbol{u}} = \boldsymbol{u}$ *holds unconditionally during the iterations process, where* $\boldsymbol{u}^{k+1}$ *is used to update* $\tilde{\boldsymbol{u}}^{k+1}$ *in the algorithm.*

III. ALGORITHM IMPLEMENTATION

Our Low-Resolution Image Prior based Network (denoted by LRIP-net) is generated based on Algorithm 1, which is implemented in Python using Operator Discretization Library (ODL), the package Adler, the ASTRA Toolbox, and Tensorflow 1.8.0. Tensorflow is a toolkit for dealing with complex mathematical problems, it can be thought of as a programming system in which you represent calculations as graphs, mathematical operations as nodes, and communication multidimensional data arrays as edges of graphs. ASTRA toolbox is a MATLAB and Python toolbox of high-performance GPU primitives for 2D and 3D tomography, the ODL is a Python library for fast prototyping focusing on inverse problems and the Adler is a toolkit that can quickly implement neural network construction.

A. Network architecture

The unrolling strategy is a discriminative learning method by unrolling an iterative optimization algorithm into a hierarchical architecture. Fig. 2 depicts the network structures of low-resolution reconstruction model, we use the classical learned primal-dual reconstruction method [1] to obtain the low-resolution solution $\boldsymbol{u}_l$, for which we can also adopt other advanced learning-based methods or variational methods. Fig. 3 depicts the network structures of our LRIP-net, which has three inputs including the incomplete projection data $\boldsymbol{f}$, the system matrix A, and the reconstructed low-resolution image $\boldsymbol{u}_l$. More specifically, there are three blocks in each stage of the high-resolution reconstruction, which correspond to the three variables. As shown at the bottom of Fig. 3, each block involves a 3-layer network.

The total depth of the network depends on the number of stages contained in the network, which is chosen to balance the receptive fields and the total number of parameters. The proposed network introduces the residual structure for two reasons: 1) the residual structure makes the network easier to train and optimize because each update is only a small offset, and 2) the skip connections can alleviate gradient disappearance and gradient explosion caused by increasing the depth of deep neural networks. The non-linear activation functions are chosen as the Parametric Rectified Linear Units (PReLU) function. As displayed in Fig. 3, we set the numbers of channels in each stage as $7 \to 32 \to 32 \to 5$ for $\boldsymbol{p}$, $6 \to 32 \to 32 \to 5$ for $\tilde{\boldsymbol{u}}$ and $\boldsymbol{u}$, where the differences in the numbers are due to the dimension of inputs. The convolutions are set to be of the size 3×3 in our network. Furthermore, we choose the Xavier initialization scheme for the convolution parameters and the zero initialization for all biases. The convolution stride is set as 1 and the padding strategy is chosen as 'SAME' in the network.

B. Network loss and optimization

In the training stage, we use both Mean Squared Error (MSE) and Structural Similarity Index (SSIM) as our loss function defined below

$$\mathcal{L} = \frac{1}{L}\sum_{i=1}^{L}\Big(\mathcal{L}_{MSE}\big(\boldsymbol{u}_i, \boldsymbol{u}_i^*\big) + \mu\mathcal{L}_{SSIM}\big(\boldsymbol{u}_i, \boldsymbol{u}_i^*\big)\Big), \quad (7)$$

where $\boldsymbol{u}_i$ denotes the reconstructed image, $\boldsymbol{u}_i^*$ denotes the reference image and μ is a trade-off parameter. We assumed that both the MSE loss and SSIM loss have the same contribution. Thus, μ is fixed as $\mu = 1$ for all experiments.

Our network updates each parameter through the backpropagation of the stochastic gradient descent method in Tensorflow.

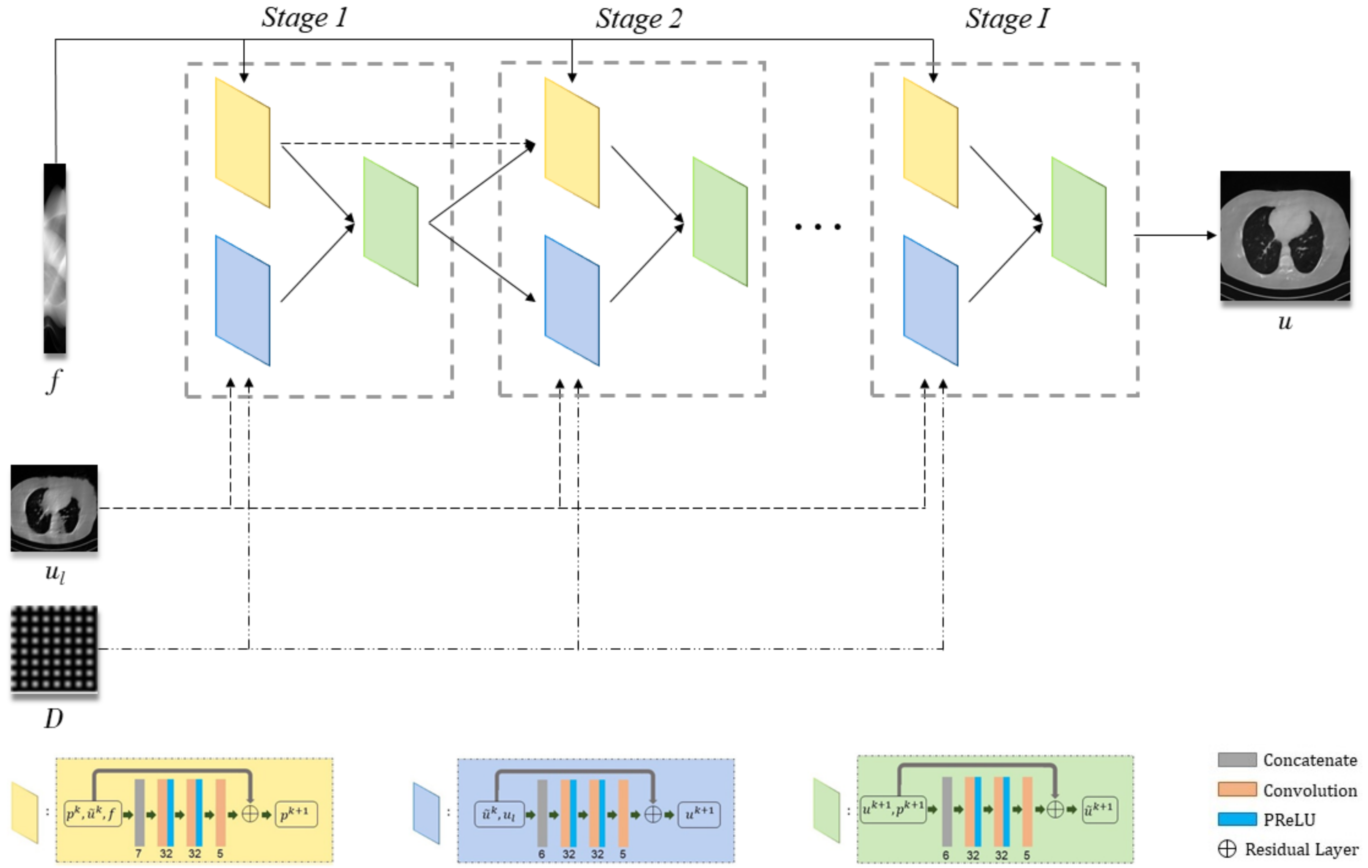

Fig. 3. The network structure of our LRIP-Net: low-resolution image prior based reconstruction model. The reconstructed image is estimated by an iterative unrolling algorithm, and each block corresponds to a variable update. The concrete structure of each block is presented at the bottom.

For a fair comparison, most experimental parameters are set as the same as the PD-net and FSR-net. We adopt the adaptive moment estimation (Adam) to optimize the learning rate by setting the parameter $\beta = 0.99$ and other parameters to their default values. The learning rate schedule is set according to cosine annealing to improve training stability, the initial learning rate η_0 is set to 10^{-4}. To further improve the training stability, the global gradient norm clipping is performed by limiting the gradient norm to 1. Besides, the batch size is set to 1 for all experiments.

IV. NUMERICAL RESULTS

In this section, we evaluate our LRIP-net on limited-angle reconstruction problems and compare it with several state-of-the-art methods on a human phantom dataset.

A. Comparison algorithms

We adopt several recent CT reconstruction methods, both the variational method and learning-based methods as given below

- TV model: *the TV regularized reconstruction model* in [33]. We tuned the balance parameter $\lambda \in [0.9, 2.5]$, the step size for the primal value $\tau \in [0.5, 0.9]$ and the step size for the dual value $\sigma \in [0.2, 0.5]$ for different experiments.
- FBP-Unet: *the FBP-Unet reconstruction* in [24]. It is a method combining the FBP reconstruction with the Unet as the post-processing to improve image quality. We use the Xavier to initialize the network parameters. And the loss function is the mean squared loss of the reconstructed image and the ground truth.
- PD-net: *the Learned Primal-Dual network* in [1]. The network is a deep unrolled neural network with 10 stages. The number of initialization channels for primal values and dual values is set to 5. The Xavier initialization and the mean squared loss of the reconstructed image and the ground truth are used in all experiments.
- SIPID: *the deep learning framework for Sinogram Interpolation and Image Denoising* in [41]. The SIPID network can achieve accurate reconstructions through alternatively training the sinogram interpolation network and the image denoising network. The Xavier initialization and the mean squared loss of the reconstructed image and the ground truth are used in all experiments.
- FSR-net: *the Learned Full-Sampling Reconstruction From Incomplete Data* in [13]. The network is an iterative expansion method that used the corresponding full-sampling projection system matrix as a prior information. To be specific, the IFSR-net guarantees the invertibility of the system matrix, while the SFSR-net guarantees numerical stability. The number of initialization channels

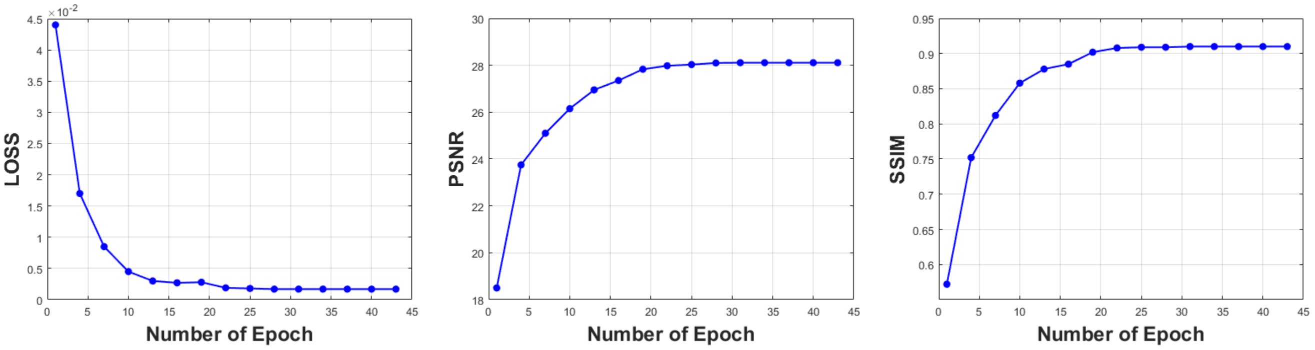

(a) Loss function (b) PSNR (c) SSIM

Fig. 4. The values of loss function, PSNR and SSIM with respect to the numbers of epochs in our network, where the curves are evaluated on the human phantom with 90° scanning angular range and 5% Gaussian noise.

for primal values and dual values is set as 6 and 7, respectively. And the loss function is the mean square error of the image domain and the Radon domain with the weight α being 1.

B. Datasets and settings

We use the clinical data "The 2016 NIH-AAPM-Mayo Clinic Low Dose CT Grand Challenge" [29], which contains 10 full-dose scans of the ACR CT accreditation phantom. We select 9 data as the training profile and leave 1 data for the evaluation, resulting in 2164 images of size 512×512 for the training and 214 images for the testing. We concern with the limited-angle reconstruction problem in the numerical experiments, for which the scanning angular interval is set as 1 degree. The additive white Gaussian noises and Poisson noises are introduced into the projected data to validate the performance of reconstruction methods.

C. Parameter behavior

In the first place, we test the effect of the number of epoch on the convergence in network training on the human dataset. The values of the loss function, PSNR, and SSIM are plotted in Fig. 4, which evidence the convergence of our LRIP-net. Accordingly to plots, we fix the number of the epochs as $k = 22$ during the training in the following experiments.

Secondly, the amount of the parameters reflects the complexity of the network. Table I lists the sizes of the parameters for the learning-based models. Because each stage in our model involves three 3-layer networks, our model has a total of 90 convolution layers, which gives 3.6×10^5 parameters. For the fairness of comparison, we set the stage number for PD-net and FSR-net to be 20 and 10, respectively.

Finally, expanding the variable space is a common network optimization technique, which allows the model to retain some memory for the variables making the training process more stable such as $\boldsymbol{u} = \left[\boldsymbol{u}^{(1)}, \boldsymbol{u}^{(2)}, \dots, \boldsymbol{u}^{(N_p)}\right]$ and $\boldsymbol{p} = \left[\boldsymbol{p}^{(1)}, \boldsymbol{p}^{(2)}, \dots, \boldsymbol{p}^{(N_d)}\right]$. In Table II, we explore the influence of the choices of N_p and N_d to reconstruction accuracy on 90° limited-angle data. As can be seen, the best accuracy is achieved with $N_p = 5$ and $N_d = 5$, which are fixed for all experiments.

TABLE I
COMPARISON OF THE PARAMETERS AMONG THE LEARNING-BASED METHODS.

Method	Number of parameters
FBP-Unet	10^7
SIPID	2×10^7
PD-net	2.4×10^5
FSR-net	4.9×10^5
LRIP-net	3.6×10^5

TABLE II
PERFORMANCE OF OUR LRIP-NET WITH RESPECT TO DIFFERENT SETTINGS OF PARAMETERS.

Settings	PSNR	RMSE	SSIM
$N_p = 4, N_d = 4$	24.7973	0.0537	0.8783
$N_p = 5, N_d = 5$	**24.9391**	**0.0528**	**0.8858**
$N_p = 6, N_d = 6$	24.8532	0.0532	0.8823
$N_p = 7, N_d = 7$	24.8349	0.0534	0.8816

D. Experiments on data with Gaussian noises

In this subsection, we evaluate the performance of our LRIP-net and other methods on limited-angle raw data corrupted different noise levels. We let the default value of τ to be $\tau = 1/2$ to obtain the low-resolution image prior unless otherwise specified. And the LRIP-net trained by the MSE loss function is denoted by LRIP-net$_{\mathrm{MSE}}$.

Table III displays the quantitative results of different methods on limited-angle data corrupted by 5% Gaussian noises. The indexes used for evaluation are PSNR, RMSE, SSIM, and running time. We observe that the reconstruction qualities of all methods decrease as the scanning angle shrinks. It can be found out that LRIP-net$_{\mathrm{MSE}}$ has obvious numerical advantage compared to other comparison algorithms. After introducing the SSIM loss into the loss function, the advantage of LRIP-net$_{1/2}$ is further improved. Therefore, we suggest to use the joint loss function in implementation. Our LRIP-net$_{1/2}$ can provide better reconstruction accuracy with 0.6 dB, 0.9 dB, 0.9 dB higher PSNR than the SFSR-net on 150°, 120°, and 90° reconstruction problem, respectively. What is even more

TABLE III
COMPARISON ON THE LIMITED-ANGLE DATA CORRUPTED BY 5% GAUSSIAN NOISES IN TERMS OF PSNR, RMSE, SSIM AND RUN TIME (MS).

Noise	$\mathrm{N}_{\mathrm{view}}$	Method	PSNR	RMSE	SSIM	Time
5%	150°	FBP	13.5911	0.1162	0.4854	**776**
		TV	25.8815	0.0631	0.8091	56532
		FBP-Unet	23.8923	0.0793	0.8703	1033
		SIPID	30.3275	0.0321	0.9276	1372
		PD-net	30.3766	0.0313	0.9301	1113
		IFSR-net	30.8763	0.0296	0.9303	1429
		SFSR-net	30.9411	0.0279	0.9324	1582
		LRIP-net$_{\mathrm{MSE}}$	31.3745	0.0256	0.9404	1245
		LRIP-net$_{1/2}$	**31.5957**	**0.0247**	**0.9426**	1264
	120°	FBP	13.4418	0.1652	0.4008	**602**
		TV	23.5852	0.0802	0.7891	60032
		FBP-Unet	21.1637	0.0981	0.8072	1023
		SIPID	27.0428	0.0416	0.9024	1346
		PD-net	27.1539	0.0402	0.9037	1132
		IFSR-net	28.0441	0.0385	0.9079	1417
		SFSR-net	28.3263	0.0372	0.9103	1551
		LRIP-net$_{\mathrm{MSE}}$	29.1888	0.0331	0.9354	1242
		LRIP-net$_{1/2}$	**29.2763**	**0.0326**	**0.9361**	1256
	90°	FBP	13.0314	0.2260	0.3881	**430**
		TV	19.9501	0.0997	0.6918	54917
		FBP-Unet	18.5181	0.1035	0.7481	1015
		SIPID	22.7492	0.0626	0.8626	1363
		PD-net	22.6047	0.0638	0.8612	1099
		IFSR-net	23.9399	0.0572	0.8744	1382
		SFSR-net	24.2494	0.0566	0.8761	1525
		LRIP-net$_{\mathrm{MSE}}$	24.9391	0.0528	0.8858	1218
		LRIP-net$_{1/2}$	**25.1555**	**0.0516**	**0.8893**	1247

TABLE IV
COMPARISON BETWEEN THE PD-NET AND OUR LRIP-NET WITH DIFFERENT LOW-RESOLUTION IMAGE PRIORS ON THE LIMITED-ANGLE DATA CORRUPTED BY 5% GAUSSIAN NOISES.

$\mathrm{N}_{\mathrm{view}}$	Method	PSNR	RMSE	SSIM	Time
150°	PD-net	30.3766	0.0313	0.9301	**1113**
	LRIP-net$_{1/2}$	31.5957	0.0247	0.9426	1264
	LRIP-net$_{1/4}$	32.7354	0.0231	0.9499	1240
	LRIP-net$_{1/8}$	**32.8775**	**0.0218**	**0.9516**	1231
	LRIP-net$_{1/16}$	32.3513	0.0241	0.9463	1227
	LRIP-net$_{1/32}$	31.5741	0.0253	0.9417	1124
120°	PD-net	27.1539	0.0402	0.9037	**1132**
	LRIP-net$_{1/2}$	29.2763	0.0326	0.9342	1256
	LRIP-net$_{1/4}$	30.0991	0.0313	0.9361	1239
	LRIP-net$_{1/8}$	**30.8746**	**0.0286**	**0.9399**	1227
	LRIP-net$_{1/16}$	30.2761	0.0306	0.9378	1217
	LRIP-net$_{1/32}$	28.9642	0.0358	0.9314	1211
90°	PD-net	22.6047	0.0638	0.8612	**1099**
	LRIP-net$_{1/2}$	25.1555	0.0516	0.8893	1247
	LRIP-net$_{1/4}$	25.9716	0.0484	0.9041	1205
	LRIP-net$_{1/8}$	**26.3553**	**0.0451**	**0.9117**	1186
	LRIP-net$_{1/16}$	26.0759	0.0477	0.9068	1175
	LRIP-net$_{1/32}$	25.2476	0.0501	0.8934	1169

important, compared to the SFSR-net, which is a dual-domain reconstruction method introducing the full-sampling system matrix as the prior knowledge, our model not only improves the reconstruction quality but also saves the computational time.

Fig. 5 presents the reconstruction results and residual images obtained by different methods for 90° limited-angle reconstruction. As can be seen, the learning-based methods outperform the direct method and TV model, which exhibit serious artifacts in the missing angle region. Although the denoiser introduced by the FBP-Unet can somehow deal with the noises, the result still presents obvious artifacts. Compared to the SIPID, PD-net and FSR-nets, our LRIP-net$_{1/2}$ can better preserve the image details and edges with less information left in the residual images. Thus, both the quantitative and qualitative results confirm that the low-to-high double-resolution strategy can improve the reconstruction accuracy for the limited-angle reconstruction problem.

As shown by Table III, the low-resolution image prior works well on limited-angle reconstruction problems. However, there is one issue left that how to choose the optimal down-sampling rate to obtain the best performance. To make it clearly, we compare the reconstruction results of our LRIP-net with respect to different low-resolution priors, which are obtained by the down-sampling rate of 1/2, 1/4, 1/8, 1/16 and 1/32, respectively. As shown in Fig. 6, the reconstruction quality of our LRIP-net first increases and then decreases as the down-sampling rate keeps decreases with the best reconstruction results provided by the down-sampling rate of $1/8$ for 150°, 120° and 90° limited-angle reconstruction. The reason behind is that the quality of the low-resolution image prior also degrades as the down-sampling rate becomes smaller and smaller, which means there is a trade-off between the resolution and quality of the low-resolution image prior. Even though, our LRIP-net has the dominant advantages compared to PD-net, which is built up by the reconstruction model without low-resolution image prior. As can be seen from Table IV, no matter what the down-sampling rate is, our LRIP-net always has significant advantages over the PD-net. The visual comparison on 90° limited-angle reconstruction are provided in Fig. 7, where our reconstructions have smoother edges and better details than PD-net.

We further increase the noise level contained in the raw data to 10% white Gaussian noises and list the quantitative results in Table V. It can be observed that the reconstruction performance of the TV model is poor in the case of high-level noises with PSNR dropping by 4 to 5 dB compared to the previous experiments. On the other hand, the performance of the learning-based methods is less sensitive to noises. The SIPID method relying on the sinogram interpolation works better than FBP-Unet. And the deep unrolling methods (i.e., PD-net, IFSR-net, SFSR-net) outperform the traditional iterative algorithm when the scanning range is limited and data is corrupted by noises. Similar to the previous experiments, compared with other deep learning algorithms, our LRIP-nets give the reconstruction results with higher PSNR and SSIM. Moreover, the low-resolution image obtained by the projection data down-sampled with rate 1/8 always gives the best reconstruction results with more than 2 dB PSNR and 0.05

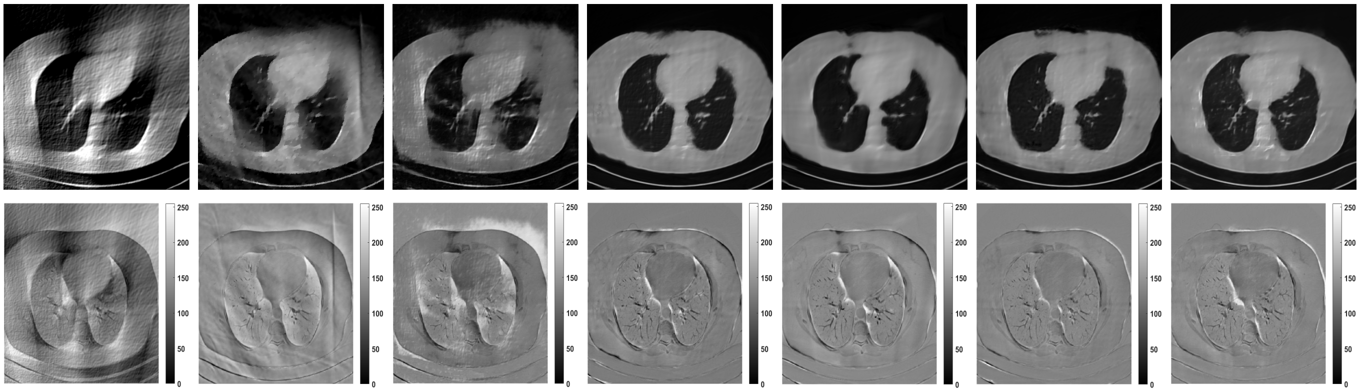

(a) FBP (b) TV (c) FBP-Unet (d) SIPID (e) PD-net (f) SFSR-net (g) LRIP-net$_{1/2}$

Fig. 5. Limited-angle reconstruction experiment of the AAPM phantom dataset with 90° scanning angular range and 5% Gaussian noises. Top row: the reconstructed images by different methods. Bottom row: the associated residual images. The display window is set as $[0, 1]$.

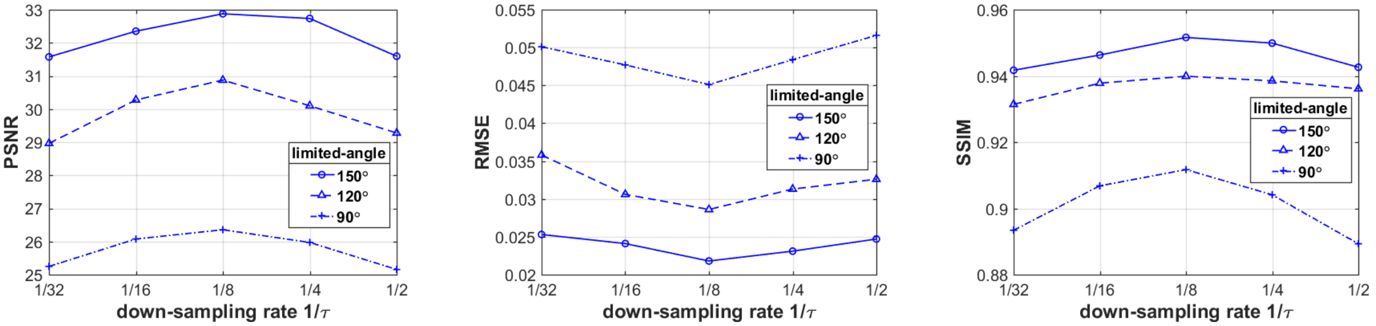

(a) PSNR (b) RMSE (c) SSIM

Fig. 6. Comparisons of PSNR, RMSE and SSIM for the limited-angle reconstruction experiments on the AAPM phantom dataset corrupted by 5% Gaussian noises, where the down-sampling rate is chosen as 1/2, 1/4, 1/8, 1/16 and 1/32, respectively, to generate the low-resolution image prior.

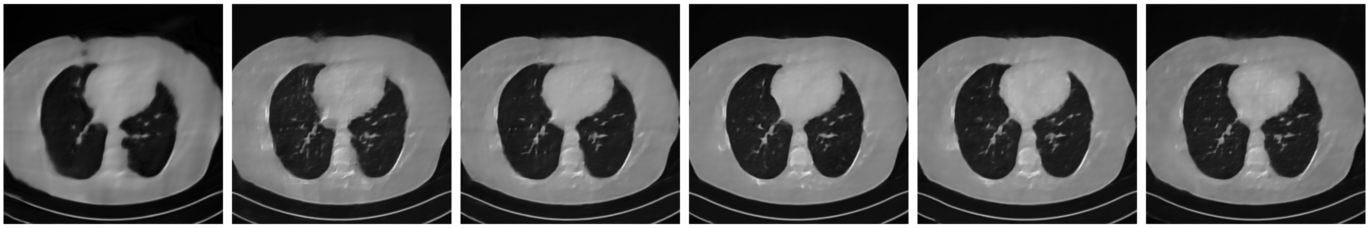

(a) PD-net (b) LRIP-net$_{1/2}$ (c) LRIP-net$_{1/4}$ (d) LRIP-net$_{1/8}$ (e) LRIP-net$_{1/16}$ (f) LRIP-net$_{1/32}$

Fig. 7. The visual comparison between the PD-net and our LRIP-net with low-resolution image prior of different resolutions on the limited-angle problem with 5% Gaussian noises and 90° scanning angular range. The display window is set as $[0, 1]$.

SSIM increments compared to the PD-net. Fig. 8 illustrates the reconstructed images from different methodologies with scanning angular range of 90° and 10% Gaussian noises. It can be seen that the both TV model and the FBP-Unet suffers from significant artifacts, which present distortions in the angular range of the missing scan. Other learning-based methods provides better visual qualities than FBP-Unet, and our LRIP-net$_{1/8}$ still gives the best reconstruction result with correct boundaries and fine structures.

E. Experiments on data with Poisson noises

Due to the statistical error of low photon counts, Poisson noises are introduced and result in random thin bright and dark streaks that appear preferentially along the direction of the greatest attenuation [15]. Table VI lists the PSNR, RMSE, and SSIM of different methods on raw data scanned within a limited scanning angle and corrupted by Poisson noises, where Poisson noises correspond to 100 incident photons per pixel before attenuation. Unlike white Gaussian noises, the performance of the TV model is significantly better than the post-processing learning method FBP-Unet. And all other learning-based methods work better than the TV model in terms of

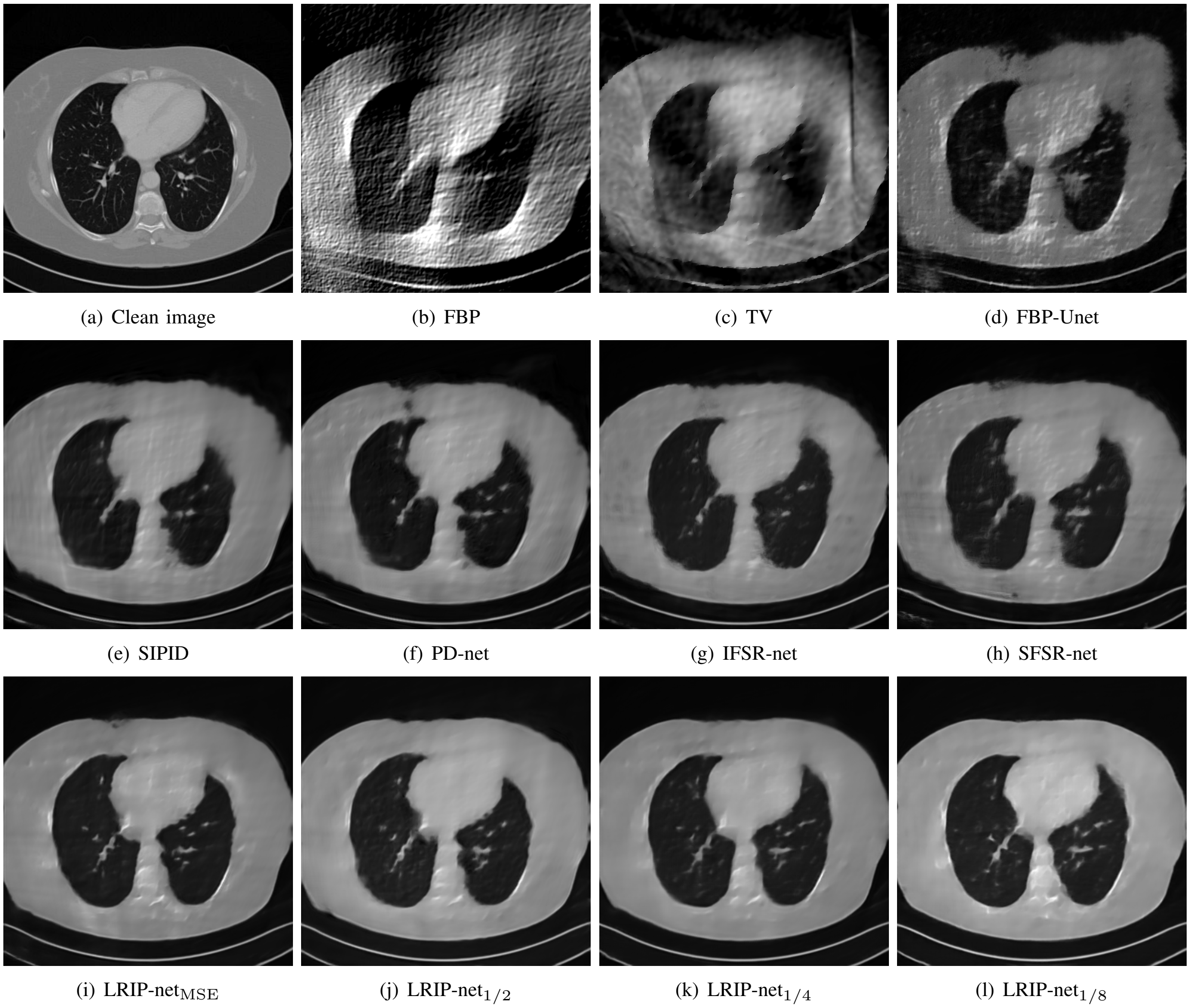
(a) Clean image (b) FBP (c) TV (d) FBP-Unet

(e) SIPID (f) PD-net (g) IFSR-net (h) SFSR-net

(i) LRIP-net$_{\mathrm{MSE}}$ (j) LRIP-net$_{1/2}$ (k) LRIP-net$_{1/4}$ (l) LRIP-net$_{1/8}$

Fig. 8. Limited-angle reconstruction experiments on the AAPM phantom dataset within 90° scanning angular range and 10% Gaussian noises. The display window is set as $[0, 1]$.

PSNR, RMSE and SSIM. Our LRIP-nets still provide the best reconstruction accuracy among all the learning-based methods for the scanning angle of $150°$, $120°$, and $90°$, respectively. It demonstrates that the LRIP-nets are also effective for data contaminated by Poisson noises.

Fig. 9 manifests the reconstruction results of these methods with scanning angular of $90°$. It can be seen that both FBP and FBP-Unet produce serious artifacts within the range of missing angles. The TV model performs well in removing Poisson noises, but it can not handle the artifacts very well. Similarly, there left obvious artifacts on boundaries and different degrees of missing in visceral tissues of the reconstruction images obtained by the SIPID, PD-net and FSR-net. The visceral tissue and boundaries of our LRIP-net reconstructions are more intact and smoother, especially for the LRIP-net$_{1/8}$ which gives the ideal boundaries. The observation becomes even apparent if we look at the zoom-in regions, where the LRIP-nets can produce results with fine structures. Therefore, we conclude that the low-resolution image prior can effectively improve the qualities of the limited-angle CT reconstruction.

As far as the running time is concerned, since the FBP is an analytical reconstruction algorithm, it gives the fastest speed. On the other, the TV model is a traditional iterative method, for which the running time is the longest. For the deep learning-based methods, the running time increases with the complexity of the network, but the overall difference is not significant.

F. Discussions

The primal-dual network can be regarded as our model without the low-resolution image prior. By comparing the results in Table III, V and VI, even though both LRIP-net and PD-net are trained by the MSE loss, the LRIP-net shows significant advantages, always producing higher PSNR and SSIM. Through such ablation study, it is shown that the low-resolution image working as prior knowledge can effectively improve the qualities of the reconstruction images. On the other hand, we discuss the impact of the low-resolution image to our LRIP-net, where the high quality priors obtained by PD-net and poor quality priors obtained by FBP are used in

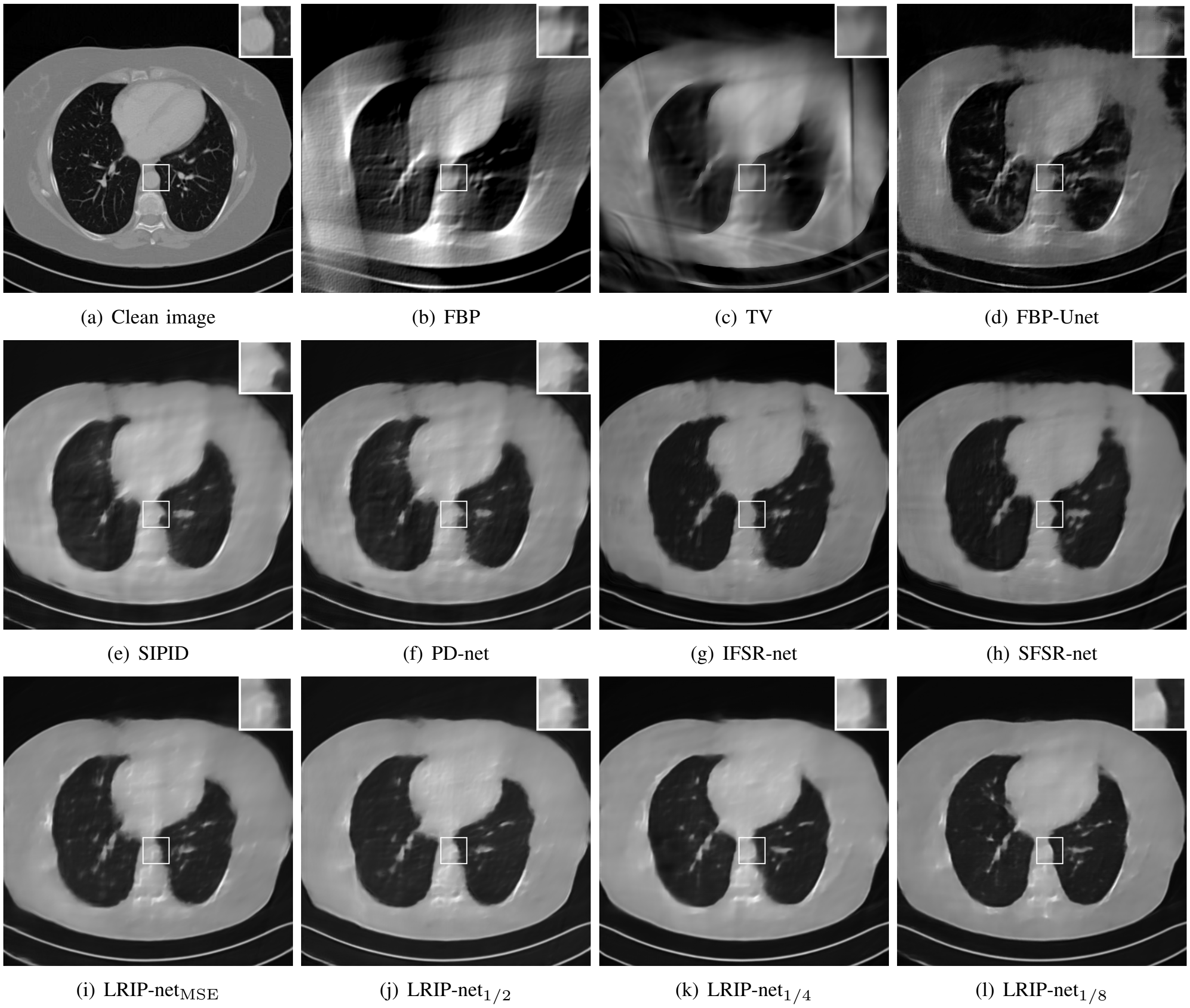
(a) Clean image (b) FBP (c) TV (d) FBP-Unet

(e) SIPID (f) PD-net (g) IFSR-net (h) SFSR-net

(i) LRIP-net$_{\mathrm{MSE}}$ (j) LRIP-net$_{1/2}$ (k) LRIP-net$_{1/4}$ (l) LRIP-net$_{1/8}$

Fig. 9. Limited-angle reconstruction experiment on the AAPM phantom dataset with 90° scanning angular range and Poisson noises. The display window is set as $[0, 1]$.

our LRIP-net. As shown in Table VII, two observations can be concluded as follows

- Our LRIP-net with the FBP reconstructed image priors always produce better reconstruction results than PD-net (see Table III). Thus, our strategy to introduce the low-resolution image as prior is not subject to the low-resolution image reconstruction method.
- Our LRIP-net with the PD-net reconstructed image priors always provide better reconstruction results than the LRIP-net using FBP reconstructed image priors. It means that the better the quality of a priori image, the better the reconstruction result.

To sum up, the low-resolution image constraint in our model (2) can help to find better solution from the null space, which has been demonstrated by our numerical experiments.

V. CONCLUSIONS AND FUTURE WORKS

In this paper, we proposed a low-resolution image prior image reconstruction model for the limited-angle reconstruction problems. The constrained model was solved by the alternating direction method with all sub-minimization problems approximated by CNN blocks, which was trained end-to-end from raw measured data. Numerical experiments on various limited-angle CT reconstruction problems have successfully demonstrated the advantages of our LRIP-net over the state-of-the-art learning methods.

Although we illustrated that the low-resolution reconstruction problem has smaller condition number than the corresponding high-resolution problem, it still lacks theoretical guarantee. Thus one future work is to investigate the observation with rigorous mathematical proof. Another possible future research direction is to use image super-resolution methods such as [16], [34] to establish more effective connection between the low-resolution and high-resolution images for solving the ill-posed CT reconstruction problems. Moreover, we also would like to develop effective methods to fuse the multi-scale information to obtain a priori image and to implement our method on other reconstruction problems such as digital breast tomosynthesis [35], which is a limited-angle

TABLE V
COMPARISON ON LIMITED-ANGLE DATA CORRUPTED BY 10% GAUSSIAN NOISES IN TERMS OF PSNR, RMSE, SSIM AND RUN TIME (MS).

Noise	N_{view}	Method	PSNR	RMSE	SSIM	Time
10%	150°	FBP	17.5464	0.1326	0.3914	**640**
		TV	20.7502	0.0917	0.5070	54536
		FBP-Unet	21.8293	0.0810	0.7887	1179
		SIPID	29.0276	0.0345	0.9193	1294
		PD-net	29.0084	0.0354	0.9193	1152
		SFSR-net	29.4543	0.0336	0.9199	1631
		IFSR-net	29.6694	0.0328	0.9231	1587
		LRIP-net$_{\mathrm{MSE}}$	30.1257	0.0304	0.9283	1390
		LRIP-net$_{1/2}$	30.3367	0.0295	0.9335	1407
		LRIP-net$_{1/4}$	30.7131	0.0291	0.9359	1386
		LRIP-net$_{1/8}$	**30.8026**	**0.0288**	**0.9362**	1375
	120°	FBP	14.8909	0.1801	0.2940	**558**
		TV	18.4345	0.1065	0.4365	55592
		FBP-Unet	20.0065	0.0999	0.7465	1207
		SIPID	26.6271	0.0461	0.8941	1311
		PD-net	26.7667	0.0458	0.8944	1221
		SFSR-net	27.2079	0.0436	0.9034	1624
		IFSR-net	27.2853	0.0432	0.9032	1539
		LRIP-net$_{\mathrm{MSE}}$	27.8333	0.0404	0.9083	1372
		LRIP-net$_{1/2}$	28.1961	0.0385	0.9196	1389
		LRIP-net$_{1/4}$	28.4371	0.0369	0.9221	1366
		LRIP-net$_{1/8}$	**29.1261**	**0.0349**	**0.9256**	1361
	90°	FBP	12.3727	0.2406	0.2455	**451**
		TV	15.9747	0.1956	0.4177	54633
		FBP-Unet	18.7582	0.1153	0.7252	1123
		SIPID	23.6216	0.0664	0.8607	1302
		PD-net	23.6473	0.0657	0.8615	1136
		SFSR-net	23.7253	0.0651	0.8591	1585
		IFSR-net	24.2056	0.0616	0.8701	1457
		LRIP-net$_{\mathrm{MSE}}$	24.5125	0.0597	0.8840	1339
		LRIP-net$_{1/2}$	24.8153	0.0576	0.8975	1356
		LRIP-net$_{1/4}$	24.9712	0.0562	0.8984	1327
		LRIP-net$_{1/8}$	**25.9377**	**0.0457**	**0.9141**	1319

TABLE VI
COMPARISON ON LIMITED-ANGLE DATA CORRUPTED BY POISSON NOISES IN TERMS OF PSNR, RMSE, SSIM AND RUN TIME (MS).

N_{view}	Method	PSNR	RMSE	SSIM	Time
150°	FBP	19.1018	0.1108	0.6626	**692**
	TV	28.4326	0.0378	0.8925	64075
	FBP-Unet	23.2040	0.0691	0.8743	1134
	SIPID	28.7649	0.0371	0.9152	1298
	PD-net	28.8137	0.0362	0.9160	1288
	IFSR-net	29.4316	0.0337	0.9236	1512
	SFSR-net	30.0356	0.0314	0.9280	1649
	LRIP-net$_{\mathrm{MSE}}$	30.2227	0.0307	0.9349	1324
	LRIP-net$_{1/2}$	30.3342	0.0303	0.9338	1341
	LRIP-net$_{1/4}$	30.8961	0.0285	0.9366	1315
	LRIP-net$_{1/8}$	**31.1291**	**0.0277**	**0.9368**	1308
120°	FBP	15.8807	0.1606	0.5243	**599**
	TV	25.3223	0.0541	0.8386	62783
	FBP-Unet	19.5694	0.1050	0.8201	1119
	SIPID	27.4079	0.0424	0.9012	1305
	PD-net	27.4054	0.0426	0.9007	1220
	IFSR-net	27.6385	0.0415	0.9107	1687
	SFSR-net	27.5545	0.0419	0.9115	1752
	LRIP-net$_{\mathrm{MSE}}$	27.7244	0.0411	0.9142	1351
	LRIP-net$_{1/2}$	27.7481	0.0409	0.9157	1367
	LRIP-net$_{1/4}$	28.4571	0.0374	0.9206	1327
	LRIP-net$_{1/8}$	**29.5724**	**0.0332**	**0.9264**	1311
90°	FBP	13.0830	0.2217	0.4747	**495**
	TV	21.5935	0.1013	0.7908	63049
	FBP-Unet	19.3228	0.1381	0.7854	1099
	SIPID	23.2017	0.0693	0.8552	1304
	PD-net	23.1127	0.0698	0.8546	1130
	IFSR-net	23.5283	0.0666	0.8711	1560
	SFSR-net	24.0277	0.0627	0.8733	1679
	LRIP-net$_{\mathrm{MSE}}$	24.6883	0.0589	0.8803	1285
	LRIP-net$_{1/2}$	24.7223	0.0582	0.8816	1306
	LRIP-net$_{1/4}$	25.2347	0.0541	0.8892	1277
	LRIP-net$_{1/8}$	**25.9344**	**0.0505**	**0.8981**	1265

x-ray tomography technique using low-dose high-resolution projections.

ACKNOWLEDGEMENT

We would like to thank the anonymous referees for their valuable comments and helpful suggestions to improve the paper.

REFERENCES

[1] Jonas Adler and Ozan Öktem. Learned primal-dual reconstruction. *IEEE Transactions on Medical Imaging*, 37(6):1322–1332, 2018.

[2] Simon Arridge, Peter Maass, Ozan Öktem, and Carola-Bibiane Schönlieb. Solving inverse problems using data-driven models. *Acta Numerica*, 28:1–174, 2019.

[3] Daniel Otero Baguer, Johannes Leuschner, and Maximilian Schmidt. Computed tomography reconstruction using deep image prior and learned reconstruction methods. *Inverse Problems*, 36(9):094004, 2020.

[4] David Boublil, Michael Elad, Joseph Shtok, and Michael Zibulevsky. Spatially-adaptive reconstruction in computed tomography using neural networks. *IEEE Transactions on Medical Imaging*, 34(7):1474–1485, 2015.

[5] Tatiana A. Bubba, Mathilde Galinier, Matti Lassas, Marco Prato, Luca Ratti, and Samuli Siltanen. Deep neural networks for inverse problems with pseudodifferential operators: An application to limited-angle tomography. *SIAM Journal on Imaging Sciences*, 14(2):470–505, 2021.

[6] Tatiana A Bubba, Gitta Kutyniok, Matti Lassas, Maximilian März, Wojciech Samek, Samuli Siltanen, and Vignesh Srinivasan. Learning the invisible: A hybrid deep learning-shearlet framework for limited angle computed tomography. *Inverse Problems*, 35(6):064002, 2019.

[7] A. Cai, L. Wang, H. Zhang, B. Yan, and J. Li. Edge guided image reconstruction in linear scan CT by weighted alternating direction TV minimization. *J Xray Sci Technol*, 22(3):335–349, 2014.

[8] Ailong Cai, Lei Li, Zhizhong Zheng, Linyuan Wang, and Bin Yan. Block-matching sparsity regularization-based image reconstruction for low-dose computed tomography. *Medical Physics*, 45(6):2439–2452, April 2018.

[9] E.J. Candes, J. Romberg, and T. Tao. Robust uncertainty principles: exact signal reconstruction from highly incomplete frequency information. *IEEE Transactions on Information Theory*, 52(2):489–509, February 2006.

[10] Guang-Hong Chen, Jie Tang, and Shuai Leng. Prior image constrained compressed sensing (PICCS): A method to accurately reconstruct dynamic CT images from highly undersampled projection data sets. *Medical Physics*, 35(2):660–663, January 2008.

[11] Hu Chen, Yi Zhang, Yunjin Chen, Junfeng Zhang, Weihua Zhang, Huaiqiang Sun, Yang Lv, Peixi Liao, Jiliu Zhou, and Ge Wang. LEARN: Learned experts' assessment-based reconstruction network for sparse-

TABLE VII
COMPARISON ON LIMITED-ANGLE DATA CORRUPTED BY 5% GAUSSIAN NOISES IN TERMS OF PSNR, RMSE, AND SSIM.

Settings	150°			120°			90°		
Method	PSNR	RMSE	SSIM	PSNR	RMSE	SSIM	PSNR	RMSE	SSIM
LRIP-net$_{1/2}$-FBP	31.1571	0.0267	0.9374	28.6398	0.0369	0.9279	24.5943	0.0545	0.8814
LRIP-net$_{1/2}$-PDnet	31.5957	0.0247	0.9426	29.2763	0.0326	0.9385	25.1555	0.0516	0.8893

data CT. *IEEE Transactions on Medical Imaging*, 37(6):1333–1347, 2018.

[12] Zhiqiang Chen, Xin Jin, Liang Li, and Ge Wang. A limited-angle CT reconstruction method based on anisotropic tv minimization. *Physics in Medicine & Biology*, 58(7):2119, 2013.

[13] Weilin Cheng, Yu Wang, Hongwei Li, and Yuping Duan. Learned full-sampling reconstruction from incomplete data. *IEEE Transactions on Computational Imaging*, 6:945–957, 2020.

[14] Qiaoqiao Ding, Gaoyu Chen, Xiaoqun Zhang, Qiu Huang, Hui Ji, and Hao Gao. Low-dose CT with deep learning regularization via proximal forward–backward splitting. *Physics in Medicine & Biology*, 65(12):125009, 2020.

[15] I.A. Elbakri and J.A. Fessler. Statistical image reconstruction for polyenergetic x-ray computed tomography. *IEEE Transactions on Medical Imaging*, 21(2):89–99, 2002.

[16] Faming Fang, Juncheng Li, and Tieyong Zeng. Soft-edge assisted network for single image super-resolution. *IEEE Transactions on Image Processing*, 29:4656–4668, 2020.

[17] Jürgen Frikel. Sparse regularization in limited angle tomography. *Applied and Computational Harmonic Analysis*, 34(1):117–141, January 2013.

[18] Alexandre Goy, Girish Rughoobur, Shuai Li, Kwabena Arthur, Akintunde I. Akinwande, and George Barbastathis. High-resolution limited-angle phase tomography of dense layered objects using deep neural networks. *Proceedings of the National Academy of Sciences*, 116(40):19848–19856, September 2019.

[19] Harshit Gupta, Kyong Hwan Jin, Ha Q Nguyen, Michael T McCann, and Michael Unser. CNN-based projected gradient descent for consistent CT image reconstruction. *IEEE Transactions on Medical Imaging*, 37(6):1440–1453, 2018.

[20] Yoseob Han and Jong Chul Ye. Framing U-net via deep convolutional framelets: Application to sparse-view CT. *IEEE Transactions on Medical Imaging*, 37(6):1418–1429, 2018.

[21] Ji He, Yan Yang, Yongbo Wang, Dong Zeng, Zhaoying Bian, Hao Zhang, Jian Sun, Zongben Xu, and Jianhua Ma. Optimizing a parameterized plug-and-play ADMM for iterative low-dose CT reconstruction. *IEEE Transactions on Medical Imaging*, 38(2):371–382, February 2019.

[22] Dianlin Hu, Yikun Zhang, Jin Liu, Changping Du, Jinglin Zhang, Shouhua Luo, Guotao Quan, Qiegen Liu, Yang Chen, and Limin Luo. Special: Single-shot projection error correction integrated adversarial learning for limited-angle CT. *IEEE Transactions on Computational Imaging*, 7:734–746, 2021.

[23] Dianlin Hu, Yikun Zhang, Jin Liu, Shouhua Luo, and Yang Chen. Dior: Deep iterative optimization-based residual-learning for limited-angle CT reconstruction. *IEEE Transactions on Medical Imaging*, 41(7):1778–1790, 2022.

[24] Kyong Hwan Jin, Michael T. McCann, Emmanuel Froustey, and Michael Unser. Deep convolutional neural network for inverse problems in imaging. *IEEE Transactions on Image Processing*, 26(9):4509–4522, September 2017.

[25] Jakob S. Jorgensen, Emil Y. Sidky, and Xiaochuan Pan. Quantifying admissible undersampling for sparsity-exploiting iterative image reconstruction in x-ray CT. *IEEE Transactions on Medical Imaging*, 32(2):460–473, February 2013.

[26] Eunhee Kang, Junhong Min, and Jong Chul Ye. A deep convolutional neural network using directional wavelets for low-dose x-ray CT reconstruction. *Medical Physics*, 44(10):e360–e375, 2017.

[27] Wei-An Lin, Haofu Liao, Cheng Peng, Xiaohang Sun, Jingdan Zhang, Jiebo Luo, Rama Chellappa, and Shaohua Kevin Zhou. Dudonet: Dual domain network for CT metal artifact reduction. In *Proceedings of the IEEE/CVF Conference on Computer Vision and Pattern Recognition*, pages 10512–10521, 2019.

[28] M. Lustig, D.L. Donoho, J.M. Santos, and J.M. Pauly. Compressed sensing MRI. *IEEE Signal Processing Magazine*, 25(2):72–82, March 2008.

[29] McCollough et al. Low-dose CT for the detection and classification of metastatic liver lesions: results of the 2016 low dose CT grand challenge. *Medical Physics*, 44(10):e339–e352, 2017.

[30] S. Niu, Y. Gao, Z. Bian, J. Huang, W. Chen, G. Yu, Z. Liang, and J. Ma. Sparse-view x-ray CT reconstruction via total generalized variation regularization. *Physics in Medicine & Biology*, 59(12):2997, 2014.

[31] Daniel Maria Pelt and Kees Joost Batenburg. Fast tomographic reconstruction from limited data using artificial neural networks. *IEEE Transactions on Image Processing*, 22(12):5238–5251, 2013.

[32] Ludwig Ritschl, Frank Bergner, Christof Fleischmann, and Marc Kachelrieß. Improved total variation-based CT image reconstruction applied to clinical data. *Physics in Medicine & Biology*, 56(6):1545–1561, February 2011.

[33] E. Y. Sidky and X. Pan. Image reconstruction in circular cone-beam computed tomography by constrained, total-variation minimization. *Physics in Medicine & Biology*, 53(17):4777, 2008.

[34] Zhaoyang Song, Xiaoqiang Zhao, Yongyong Hui, and Hongmei Jiang. Progressive back-projection network for COVID-CT super-resolution. *Computer Methods and Programs in Biomedicine*, 208:106193, 2021.

[35] Jonas Teuwen, Nikita Moriakov, Christian Fedon, Marco Caballo, Ingrid Reiser, Pedrag Bakic, Eloy García, Oliver Diaz, Koen Michielsen, and Ioannis Sechopoulos. Deep learning reconstruction of digital breast tomosynthesis images for accurate breast density and patient-specific radiation dose estimation. *Medical Image Analysis*, 71:102061, 2021.

[36] Chao Wang, Min Tao, James G. Nagy, and Yifei Lou. Limited-angle CT reconstruction via the L1/L2 minimization. *SIAM Journal on Imaging Sciences*, 14(2):749–777, 2021.

[37] Jiaxi Wang, Chengxiang Wang, Yumeng Guo, Wei Yu, and Li Zeng. Guided image filtering based limited-angle CT reconstruction algorithm using wavelet frame. *IEEE Access*, 7:99954–99963, 2019.

[38] Tobias Würfl, Mathis Hoffmann, Vincent Christlein, Katharina Breininger, Yixin Huang, Mathias Unberath, and Andreas K Maier. Deep learning computed tomography: Learning projection-domain weights from image domain in limited angle problems. *IEEE Transactions on Medical Imaging*, 37(6):1454–1463, 2018.

[39] Jinqiu Xu, Yunsong Zhao, Hongwei Li, and Peng Zhang. An image reconstruction model regularized by edge-preserving diffusion and smoothing for limited-angle computed tomography. *Inverse Problems*, 35(8):085004, July 2019.

[40] Moran Xu, Dianlin Hu, Fulin Luo, Fenglin Liu, Shaoyu Wang, and Weiwen Wu. Limited-angle x-ray CT reconstruction using image gradient ℓ_0-norm with dictionary learning. *IEEE Transactions on Radiation and Plasma Medical Sciences*, 5(1):78–87, 2021.

[41] Huizhuo Yuan, Jinzhu Jia, and Zhanxing Zhu. Sipid: A deep learning framework for sinogram interpolation and image denoising in low-dose CT reconstruction. In *2018 IEEE 15th International Symposium on Biomedical Imaging (ISBI 2018)*, pages 1521–1524, 2018.

[42] Guangming Zang, Ramzi Idoughi, Rui Li, Peter Wonka, and Wolfgang Heidrich. Intratomo: Self-supervised learning-based tomography via sinogram synthesis and prediction. In *Proceedings of the IEEE/CVF International Conference on Computer Vision (ICCV)*, pages 1960–1970, October 2021.

[43] H. Zhang, L. Wang, Y. Duan, L. Lei, G. Hu, and B. Yan. Euler's elastica strategy for limited-angle computed tomography image reconstruction. *IEEE Transactions on Nuclear Science*, 64(8):2395–2405, 2017.

[44] Haimiao Zhang, Bin Dong, and Baodong Liu. Jsr-net: a deep network for joint spatial-radon domain CT reconstruction from incomplete data. In *ICASSP 2019-2019 IEEE International Conference on Acoustics, Speech and Signal Processing (ICASSP)*, pages 3657–3661. IEEE, 2019.